A peridynamic model for damage and fracture in porous materials

Ziguang Chen[1,2], Sina Niazi[3], Florin Bobaru[3*]

[1]Department of Mechanics, Huazhong University of Science and Technology, Wuhan, 430074, China

[2]Hubei Key Laboratory of Engineering Structural Analysis and Safety Assessment, 1037 Luoyu Road, 430074, Wuhan, China

[3]Department of Mechanical and Materials Engineering, University of Nebraska-Lincoln, Lincoln, Nebraska 68588-0526, USA

*Corresponding author's E-mail address: fbobaru2@unl.edu

Abstract:

We introduce a peridynamic (PD) model for simulating damage and fracture in porous materials based on an Intermediate Homogenization (IH) approach. In this approach, instead of explicitly representing the detailed pore geometry, we use homogenization but maintain some information about the microstructure (porosity) in the model. Porosity is introduced in the model as initial peridynamic damage, implemented by stochastically pre-breaking peridynamic bonds to match the desired porosity value. We validate the model for elastodynamics with wave propagation in porous glasses, where we match observed wave propagation speeds and the apparent elastic moduli for various porosities. The model is then used to study the fracture behavior of Berea sandstone under three-point bending loading conditions. We validate the model for fracture problems using the case of failure in a sandstone sample with an off-center pre-notch under three-point bending. The IH-PD results agree very well with experiments: we obtain different failure modes depending on the length of the off-center pre-notch. When the pre-notch is short, most damage (and the subsequent

failure) happens in the center of the beam (largest tensile stresses in an un-notched sample). In this case, material porosity makes the fracture behavior "insensitive" to the presence of the off-center pre-notch. When the pre-notch is long, damage starts from near its tip, and progresses in mixed mode towards the loading point. The model captures the location of crack initiation to be the right-corner of the notch, exactly as shown by the experimental acoustic emission results. A fully-homogenized model for the porous sandstone fails to reproduce the failure mode sensitivity on the pre-notch length. The results show the importance of using the IH-PD model when trying to capture the important effects local heterogeneities (like pores) have on damage initiation and growth in porous materials.

Keywords: Porous materials; Porosity; Peridynamics; Fracture; Rock; Damage.

1. Introduction

Damage and fracture in natural or man-made porous materials (bone, wood, rock, sandstone, or metal foams, filters, concrete, composites, ceramics) present particular challenges: damage can be widespread or finely localized, as micro-cracks "jump" over pores and link together into a number of macro-cracks leading to final failure or they stay separated leading to micro-crushing and eventual large scale fragmentation. The underlying physical principles governing their mechanical behavior, but not their failure behavior, is known as "poromechanics".[1-3] Poroelastic media are elastic materials with pores/voids of arbitrary shapes and sizes, usually randomly distributed and oriented through the material. Many porous materials can be considered as elastic quasi-brittle materials, as least locally. Their global failure response can, sometimes, appear as ductile failure, as locally brittle damage spreads over pores, flaws and other kinds of discontinuities. The geometry and distribution of pores have a close relationship to their

mechanical properties, such as mechanical strength, Young's modulus, permeability and sonic velocity.[4-7] Many constitutive models have been proposed to investigate and predict elastic properties of porous materials, for instance: Voigt, Reuss, Wood, Hashin-Shtrikman (HS), Gassmann, Modified Voigt and Modified HS models.[5] These poromechanical models capture the dependence of apparent, or effective, elastic properties on porosity; they do not, however, say anything about the dependence of "effective" fracture and damage properties on pores.[8] Our goal is to introduce a model which can directly capture the influence of porosity on the fracture and damage evolution, without the need of the explicitly modeling the porous geometry.

Damage initiation, progression, and final failure in rock, a porous material, is an important topic in rock engineering, hydraulic fracturing, and mining sciences. Substantial efforts, experimental, theoretical, and computational, have been dedicated to studying damage evolution in rock under various loadings.[9-11] Some recent computational methods have been helpful in predicting the initiation and propagation of cracks in porous materials, especially rocks.[12] Two main types of computational models have been used to investigate damage and fracture in porous materials: models that use a detailed description of the microstructure geometry, and homogenized approaches. The explicit microstructure models involve either digitized porous microstructures from experimental images, or generated by researchers to mimic actual ones. These models have severe limitations in terms of the size of the sample that can be modeled, due to the high computational cost. When the sample size is much larger than the pore size, it is computationally unfeasible to consider the exact geometry and location for every single pore.[2] Consequently, averaged, or "homogenized" models have been used as an alternative for simulating porous materials' behavior under mechanical loading conditions.[13, 14] These homogenization approaches, however, may not be able to capture the strong influence local heterogeneities have on damage

initiation and crack propagation. Although many continuum-based and discontinuous (e.g. distinct element method) methods based on classically homogenized poromechanical approaches have been developed and applied to model porous materials fracture, it remains an open question whether they can correctly capture their fracture behavior.[12]

A compromise between having a low computational cost (on par with that of homogenized models) and being able to reproduce the effects the porous microstructure has on the initiation and propagation of fracture and damage is sought in the present contribution. For this purpose, we introduce an intermediately-homogenized peridynamic (IH-PD) model and validate it against experimental results for wave propagation in porous media of different porosities. We then test the new model on Berea sandstone fracture from a three-point bending setup with an off-center pre-notch. Experiments show that the sample fails from the pre-notch if the notch is sufficiently long, but if the notch is short, the porous stone fails from its center (the point of maximum tensile stress of an un-notched specimen). We compare the results from the IH-PD model with those from experiments, with other methods from the literature, and with a fully-homogenized peridynamic model. We comment on the results obtained and discuss the importance of preserving the effect of local heterogeneities on the damage initiation, distribution, and crack propagation. This can be accomplished with the new IH-PD model, and at a similar cost with a fully homogenized peridynamic model. Fully homogenized models (classical or peridynamics-based), however, lose important heterogeneity information that controls crack initiation and propagation and because of that will miss, in a significant way, the correct failure behavior of porous materials. Therein lie the benefits for the proposed modeling approach we present in this paper.

2. Literature review

Peridynamics, a new nonlocal continuum theory proposed by Stewart Silling,[15, 16] eliminates spatial derivatives from the classical formulation of continuum mechanics, which makes it a consistent mathematical model for problems with discontinuities in the displacement field. The model is particularly well suited for dealing with cracks and damage in solid mechanics especially in situations where the crack path is not known in advance. These features have enabled peridynamics to be successfully applied to diverse engineering problems that involve fracture and damage evolution.[17-23]

Several recent studies have applied peridynamics in porous materials-related problems: Katiyar et al.[24] and later Jabakhanji and Mohtar[25] developed a peridynamic approach to model flow in porous media. Peridynamics was also used to address hydraulic fracturing and reproduce the deformation induced by the fluid flow in a porous medium.[26-28]

In the present study, we focus on the initiation and propagation of cracks in dry porous rock. Recently, Zhou et al. investigated how complex fracturing patterns initiate and propagate from a single flaw embedded in rock-like materials under compression using bond-based peridynamics.[29] With this homogeneous PD model, Zhou and co-authors simulated crack propagation in rocks with pre-existing flaws (e.g.[30-32]). These PD models, when applied to failure of materials with relatively high porosity, would have the same issues as the fully-homogenized PD model discussed in section 5. Lee et al. applied bond-based peridynamics to understand crack coalescing processes in rock materials.[33] In these studies of rock fracture, the actual rock materials studied are dense materials with small porosity, such as marble[29] (porosity: 2%[34]), and Longtan sandstone[14] (porosity: 1.38%[35]). When the porosity is not negligible, such as in Berea sandstone

(porosity range: 10.2~22.2%[36-38]), damage initiation and crack propagation are strongly influenced by it. As we shall see in section 5, this aspect limits the applicability of such homogenized models.

3. Peridynamic model for porous materials

In this section, we first briefly review the peridynamic theory for elastic brittle materials. Then, we describe the fully homogenized PD model (FH-PD) and introduce the new Intermediately Homogenized PeriDynamic (IH-PD) model for porous materials.

3.1. Brief review of peridynamic theory for elastic brittle materials

The peridynamic model is a framework for continuum mechanics based on the idea that pairs of material points exert forces on each other across a finite distance. This concept allows for the natural evolution (initiation, propagation, and interaction) of damage and cracks and can be viewed as an effective treatment of material length-scale induced by, for example, the material microstructure. The peridynamic equations of motion for the bond-based model are given as:[15]

$$\rho\ddot{\boldsymbol{u}}(\boldsymbol{x},t) = \int_{H_x} \boldsymbol{f}\big(\hat{\boldsymbol{x}} - \boldsymbol{x}, \boldsymbol{u}(\hat{\boldsymbol{x}},t) - \boldsymbol{u}(\boldsymbol{x},t)\big)\,\mathrm{d}V_{\hat{\boldsymbol{x}}} + \boldsymbol{b}(\boldsymbol{x},t)\,, \tag{1}$$

where $\boldsymbol{f}$ is the pairwise force function in the peridynamic bond that connects point $\hat{\boldsymbol{x}}$ to $\boldsymbol{x}$, $\boldsymbol{u}$ is the displacement vector field, ρ is the density and $\boldsymbol{b}(\boldsymbol{x},t)$ is the body force. The integral is defined over a region H_x called the "horizon region", or simply the "horizon". The horizon is the compact-supported domain of the pairwise force function around a point $\boldsymbol{x}$ (see Fig. 1). The horizon region is taken here to be a circular disk (sphere) of radius δ. We refer to δ also as the "horizon", and from the context there should be no confusion whether we refer to the region or its radius.

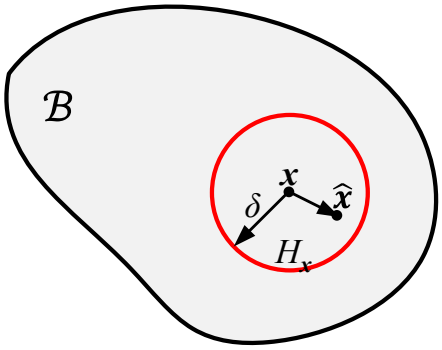

Fig. 1. Each point $\boldsymbol{x}$ interacts directly with any point $\hat{x}$ in the horizon region delimitated by the red circle.

A micro-elastic material is defined as one for which the pairwise force derives from a potential:

$$\boldsymbol{f}(\boldsymbol{\xi},\boldsymbol{\eta}) = \frac{\partial \omega(\boldsymbol{\xi},\boldsymbol{\eta})}{\partial \boldsymbol{\eta}}, \tag{2}$$

where $\boldsymbol{\xi} = \hat{\boldsymbol{x}} - \boldsymbol{x}$ is the relative position in the reference configuration and $\boldsymbol{\eta} = \boldsymbol{u}(\hat{\boldsymbol{x}}, t) - \boldsymbol{u}(\boldsymbol{x}, t)$ is the relative displacement between $\boldsymbol{x}$ and $\hat{\boldsymbol{x}}$. A micropotential that leads to a linear microelastic material is given by:

$$\omega = \frac{1}{2} c(\xi) s^2 \xi, \tag{3}$$

where $\xi = \|\boldsymbol{\xi}\|$, and $s = \frac{\|\boldsymbol{\xi}+\boldsymbol{\eta}\| - \|\boldsymbol{\xi}\|}{\|\boldsymbol{\xi}\|}$ is the relative elongation of a bond, or bond strain. The function $c(\xi)$ is called the micro-modulus and has the meaning of bond's elastic stiffness. The pairwise force corresponding to the micropotential given above has the following form:

$$\boldsymbol{f}(\boldsymbol{\eta},\boldsymbol{\xi}) = \begin{cases} \dfrac{\boldsymbol{\xi}+\boldsymbol{\eta}}{\|\boldsymbol{\xi}+\boldsymbol{\eta}\|} c(\xi)s & \xi \le \delta \\ \mathbf{0} & \xi > \delta \end{cases} \tag{4}$$

Following the same procedure performed to calculate the micro-modulus functions in 1D (see[40]), one obtains the conical micro-modulus function in 2D, plane stress conditions:[41]

$$c(\xi) = c_1\left(1-\frac{\xi}{\delta}\right) = \frac{36E}{\pi\delta^3}\left(1-\frac{\xi}{\delta}\right), \tag{5}$$

or, assuming a constant micro-modulus function over the horizon region, in 2D, plane stress conditions:

$$c(\xi) = \frac{9E}{\pi\delta^3}, \tag{6}$$

where E is Young's modulus of the material. In the IH-PD model of porous material, E is the elastic modulus of the constituent material of the porous medium and this is discussed in Section 3.3. The material model in Eq. (4) is equivalent to the kernel function using $n = 1$ for peridynamic kernel $c(\hat{\boldsymbol{x}},\boldsymbol{x})/|\hat{\boldsymbol{x}}-\boldsymbol{x}|^n$ by Chen et al.[42] They constructed a peridynamic kernel ($n = 2$) based on physical principles for dynamic elasticity and showed that, when the one-point Gauss quadrature is used for discretization, the $n = 2$ model is the only one whose convergence to the classical solution does not depend on the fineness of the discretization grid. Models with $n = 0$ or $n = 1$ also converge, in the limit of horizon going to zero and ratio of horizon to grid spacing going to infinity,

to the classical solution for problem with sufficient smoothness. No significant differences on crack patterns were observed between models with $n = 1$ and $n = 2$.[43] In this work we use the model with $n = 1$.

Failure is introduced in peridynamics by considering that the peridynamic bonds break when they are deformed beyond a critical value, called the critical relative elongation or critical bond strain, s_0, computed based on the material's fracture energy. In 2D, the energy per unit fracture length for complete separation of the two halves of the body is the fracture energy G_0. Equating it to the work done in a PD material to accomplish the separation of the body into two halves gives:

$$G_0 = 2\int_0^{\delta}\int_z^{\delta}\int_0^{\cos^{-1}(\frac{z}{\xi})}\left[\frac{c(\xi)s_0^2\xi}{2}\right]\xi d\theta d\xi dz\,. \tag{7}$$

Substituting the micro-modulus functions from Eqs. (5) and (6) into Eq. (7), respectively, s_0 is obtained for the conical micromodulus function (under plane stress conditions) as:

$$s_0 = \sqrt{\frac{5\pi G_0}{9E\delta}}, \tag{8}$$

and for the constant micromodulus function as:

$$s_0 = \sqrt{\frac{4\pi G_0}{9E\delta}}\,. \tag{9}$$

For the IH-PD model of poroelastic materials, G_0 is the fracture energy of the constituent material of the porous medium (see details in Section 5).

3.2. Numerical discretization

In this section we describe the numerical implementation details, including both dynamic and static solutions. In principle, the peridynamic equations can be discretized using the finite element method, or any other method appropriate to compute solutions to integro-differential equations (or integral equations for the static case). These approaches, however, soon hit well-known obstacles and difficulties for problems with evolving topologies, like those in which cracks initiate, grow, and interact with each other leading to damage, full fracture and/or fragmentation. Instead, meshfree-types discretizations are preferred for peridynamic simulations of material failure and damage. The discretization proposed by Silling and Askari[44] uses the mid-point integration scheme (equivalent to one-point Gauss quadrature) for the domain integral. Numerical simulations are performed using the following discretized equation:

$$\int_{H_{\boldsymbol{x}}} \boldsymbol{f}\big(\hat{\boldsymbol{x}} - \boldsymbol{x}_i, \boldsymbol{u}(\hat{\boldsymbol{x}}, t) - \boldsymbol{u}(\boldsymbol{x}_i, t)\big)\, \mathrm{d}V_{\hat{\boldsymbol{x}}} \simeq \sum_{j \in \mathrm{Fam}(i)} c(\xi_{ij}) s_{ij} V_{ij} \tag{10}$$

where Fam(i) is the family of nodes j with their area (volume in 3D) covered, fully or partially, by the horizon region of node i, ξ_{ij} is the bond length between nodes i and j, s_{ij} is the relative elongation for the bond connecting nodes i and j, and V_{ij} is the area of node j estimated to be covered by the horizon of node i.

Note that node j may not be fully contained within the horizon of node i, so a "partial volume" integration, first introduced by Bobaru et al[45] and also shown in their following work,[46] is used

here to improve the accuracy of the mid-point quadrature scheme. The main advantage of this algorithm compared with one that simply checks whether a node is inside or outside the horizon region is that, as the grid density increases (for a fixed horizon value), the numerical convergence (in terms of strain energy density, for example) is monotonic.[45]

For a fixed horizon, the ratio $m = \delta/\Delta x$ describes how accurate the numerical quadrature for the integral in Eq. (1) will be. We call this ratio "the horizon factor". In the convergence study shown in Section 4, we study both *m*-convergence and δ-convergence[40] for an elastic wave propagation problem. We recall that in *m*-convergence we consider the horizon δ fixed and take $m \to \infty$. The numerical PD approximation will converge in this case to the exact nonlocal PD solution for the given δ. In the case of δ-convergence, the horizon $\delta \to 0$ while *m* is fixed or increases with decreasing δ. For δ-convergence and in problems with no singularities, the numerical PD solutions are expected to converge to the classical local solution (as *m* increases).

Both dynamic (see Section 4) and static (see Section 5) simulations are performed in this work. In the dynamic simulations for elastic wave propagation in a porous glass (see Section 4), we apply the Velocity-Verlet method with a time interval of 0.1 μs. For the quasi-static fracture tests in Section 5, the energy minimization method[47, 48] is used, and the nonlinear conjugate gradient (CG) method with secant line search is adopted to minimize the strain energy of the system. For all static simulations in this paper, the nonlinear CG method is used with a convergence tolerance defined by: $\frac{|W_k - W_{k-1}|}{W_{k-1}} < 10^{-6}$, in which W_k, and W_{k-1} are the total strain energy at the current (*k*-th) and previous (*k*-th-1) CG iterations.

Substituting Eq. (10) into Eq. (1), we obtain the nonlinear system of the discretized equations for quasi-static conditions:

$$\sum_{j\in \mathrm{Fam}(i)} c(\xi_{ij}) s_{ij} V_{ij} + b_i = 0, \quad (11)$$

where b_i is the body force at node i.

3.3. An intermediately-homogenized peridynamic model for poroelastic materials

In the fully-homogenized peridynamic (FH-PD) models, heterogeneous materials are understood as material models *locally homogenized* in terms of their elastic properties, density, and fracture energy.[19] The properties used in the FH-PD models can be calculated from the constitutive models of porous materials, such as Voigt or Reuss models with known porosity and properties of the constituent material, or the apparent parameters from direct measurements. Porous materials, when the pores sizes are much smaller than the sample sizes, can also be viewed as locally homogeneous. Excellent simulation results are produced by the FH-PD models for rock with low porosity. When the rock porosity is not negligible, such as in Berea sandstone, local heterogeneities can highly influence damage initiation and crack propagation, which limits the applicability of fully-homogenized models for these cases. In this section, we introduce the intermediately-homogenized peridynamic (IH-PD) model for porous materials. The reader is referred to[49] for more details on using the IH-PD model for multi-phase materials.

Here we introduce a peridynamic model for porous materials based on an Intermediate Homogenization (IH) approach to simulate fracture and damage in such materials. The porosity is represented by peridynamic pre-damage, with mechanical bonds connected to a peridynamic node being pre-broken, stochastically, to achieve the desired porosity. The "intermediate homogenization" approach refers to the fact that we do not represent the explicit geometry of the actual pores in the material, and neither do we fully homogenize the porous medium. With the IH method we aim to maintain sufficient information about the porosity to allows us to more accurately compute the failure behavior of porous materials compared with the FH-PD. At the

same time, the IH-PD model will be significantly more efficient computationally compared with a model that uses an explicit geometric representation of the microstructural individual pores, while hopefully, still being able to compute the macro-scale failure behavior with accuracy.

In the IH-PD model of porous materials, pores are treated as pre-existing material damage. In peridynamics, the damage index is computed as the ratio between the number of broken (or failed) bonds (N_f) and the total number of bonds (N) originally associated with a node ($d(x,t) = \frac{N_f}{N}$). To mimic the presence of pores, we randomly break a number of bonds at each node (see Fig. 2). We calibrate the number of broken bonds to the material's porosity. This procedure creates a "pre-damage index", related to material's porosity and computed like the damage index above but with N_p, the number of pre-broken bonds at a node, replacing N_f. When the porosity reaches the *critical porosity* P_c (the porosity beyond which the rock can exist only as a suspension[6]), all bonds associated with that point should be broken ($N_p = N$), meaning that the pre-damage index is unity. For zero porosity, no pre-broken bonds are introduced (pre-damage index is zero at all points).

To perform the calibration for the number of pre-broken bonds, we implement the initial damage representative of the pores by adopting the ideas used in the "concentration-dependent damage" (CDD) model originally proposed by Chen and Bobaru[18] and used for modeling of damage induced by corrosion processes[50-53]. Here, we assume that the pre-damage index at a point depends linearly on its porosity when zero-porosity material surrounds the point: $d_p(\boldsymbol{x}) = P(\boldsymbol{x})/P_c$, where $P(\boldsymbol{x})$ is the given local material porosity. The algorithm for implementing the pre-damage, at a node $\boldsymbol{x}$, is:

i. For each intact bond in the family of the node, generate a random number r from a uniform distribution in (0, 1);

ii. *If r is smaller than $P(\boldsymbol{x})/P_c$, then break this bond. Since each bond connects two nodes, update the pre-damage information at both nodes;*

iii. *Go to next bond in the family of bonds of node $\boldsymbol{x}$.*

This procedure is applied for all nodes in the material. Here we assume that the pore shapes and distribution are "isotropic", therefore the peridynamic pre-damage representation of this case uses the same uniform distribution for bond-breaking independent of the node location or the bond direction. Special *location-* and/or *orientation-dependent pre-damage* can easily be introduced to mimic anisotropy in porous materials.

With the above algorithm, each PD bond (connecting material points $\boldsymbol{x}$ and $\hat{\boldsymbol{x}}$) goes through the procedure twice. If porosities at $\boldsymbol{x}$ and $\hat{\boldsymbol{x}}$ are $P(\boldsymbol{x})$ and $P(\hat{\boldsymbol{x}})$, respectively, the chance for the $\boldsymbol{x}-\hat{\boldsymbol{x}}$ bond to remain intact is $(1-P(\boldsymbol{x})/P_c)(1-P(\hat{\boldsymbol{x}})/P_c)$. For materials with uniform porosity P, the change for any bond to stay intact is: $(1-P/P_c)^2$. The pre-damage index, the ratio between the number of pre-broken bonds and the total number of bonds at a node, in this case, converges to:

$$d_p = 1-(1-P/P_c)^2 \tag{12}$$

in the limit of the horizon factor (the ratio between the horizon size and grid spacing) going to infinity (also known as the *m*-convergence, see Section 3.2). Notice the nonlinear dependency, for a material with uniform porosity, between the pre-damage index and the given porosity.

In Fig. 2b we show the computed pre-damage index value for the input *uniform* porosities of 0.1, 0.3, 0.5 and 0.7, with a critical porosity of 1. When the horizon factor goes to infinity, the *pre-damage index value*, according to Eq. (12), converges to 0.19, 0.51, 0.75 and 0.91, respectively. Observe that these values match well the dominant colors in the pre-damage index maps shown in

Fig. 2b for the particular value of the horizon size equal to 4 cm (sample size is 1 m by 1 m) and a horizon factor m=4.

In the next section, we use the IH-PD model to simulate elastic wave propagation in porous glasses. By computationally measuring the wave speeds corresponding to different porosities, we calculate the apparent elastic moduli, and compare them with those measured in experiments.

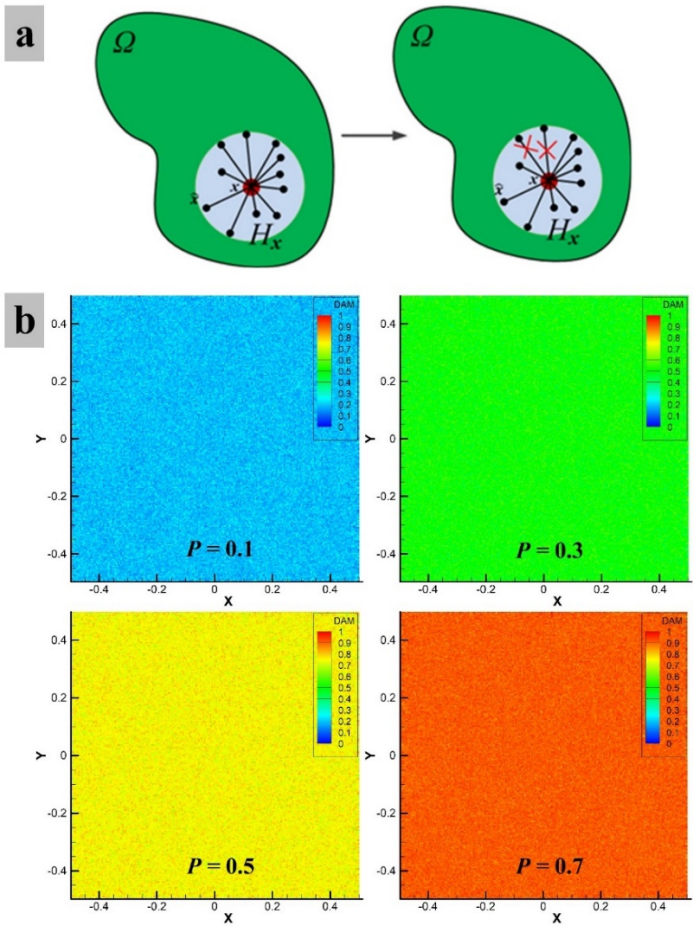

Fig. 2. Peridynamic modeling of porosity via random pre-breaking of bonds; in (b): peridynamic pre-damage maps corresponding to different given porosities: 0.1, 0.3, 0.5 and 0.7. The units for the axes is meter.

4. Model verification and validation for elasto-dynamic problems

We verify (by performing convergence studies) and validate the IH-PD model for an elasto-dynamic problem: elastic wave propagation in porous glasses. We generate elastic waves by suddenly applying a force pulse over a small region in the sample and monitor their propagation through the sample. Experimental data regarding the apparent elastic modulus of these porous glasses in terms of varying degrees of porosity exists.[54]

Fig. 3 shows the problem setting for the dynamic test with the IH-PD model. An elastic wave is induced in the porous glass (2D plane stress) sample by a sudden pulse applied (as a body force) over a region at the bottom. For zero porosity glass, elastic modulus is E = 46.1 GPa, and density ρ = 2511 kg/m^3.[54] For porous glass or glass foam, the critical porosity can be higher than 0.9.[6] Here we consider $P_C \approx 1$ for the porous glass simulations.

We test if the model can predict the experimentally measured relationship between elastic wave speed and material porosity. We arbitrarily choose a sample size of 1 m × 1 m. A suddenly applied load of 1 MPa in the vertical-up direction over the region (100 mm in length) at the bottom side is kept constant for 5 μs (see Fig. 3). After that, the load is suddenly removed. The loading generates elastic waves propagating through the sample.

Although the horizon-size-dependence of the loading region leads to wave patterns that depend on the horizon size, the wave speed does not change much with the horizon size and should converge to the measured value when the horizon size goes to zero.[40] Since our goal is to calculate the wave speeds for different porosities, the specific initial loading conditions (loading range, loading magnitude) are not important.

To compute the wave speed from the PD model results, we track the location of the pressure wave's peak over a time period that starts shortly after the pulse is applied and stops before waves

return from the sample's boundaries. More specifically, we compute an average velocity by tracking the displacement of the crossing point between line $x = 0$ (shown in Fig. 4) and the crest of the front wave, over the time period 100 μs -200 μs from the application of the pulse. For this verification phase we are interested only in the elastic wave propagation, therefore we apply a "no-fail" condition for all bonds in the model. Obviously, the pre-damage corresponding to different porosities is present in these calculations, but no "new damage" is allowed.

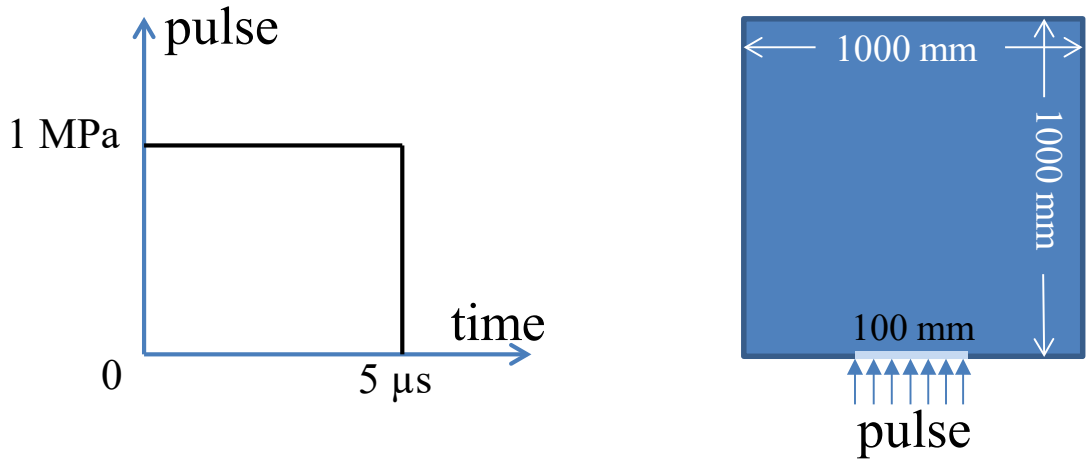

Fig. 3. The problem setting used for verification and validation of the IH-PD model for elasto-dynamic conditions. Wave propagation is induced by a suddenly applied load over the "punch" zone shown in the right figure. Left: pulse profile; Right: sample dimensions and loading location.

Fig. 4 shows the elastic waves propagating in the porous glass with the assumed porosities of $P = 0$ and 0.5, at different times: $t = 4$ μs, 40 μs, 100 μs, and 160 μs, respectively. The colors indicate the magnitude of the vertical component of the nodal velocity vector generated by the sudden pulse. For cases shown in Fig. 4, the horizon size is 40 mm, and the horizon factor m=8. One notable difference between the nonporous ($P = 0$) and the porous case (e.g., $P = 0.5$) that can be observed from these results, is that in the porous sample stress waves become less coherent, being locally dispersed ("noisier" velocity maps) by the more detailed representation (with the IH-

PD model) of the heterogeneous microstructure. When porosity (pre-damage) is higher, the possibility for material nodes in the PD model to have no connections with surrounding nodes increases, especially when the horizon factor *m* is small. Because of this, to compare the wave speeds in glass plates with different porosities, especially for high porosities such as 0.9, we need to use a sufficiently large horizon factor *m*. Here we used *m*=16.

Snapshots at 100 μs from the initial time step for the vertical component of the nodal velocities in porous glass samples are shown in Fig. 5 (Movies 1-5 display the time-evolution for the vertical component of the nodal velocity vector over the first 200 μs, showing the progression of wave propagation for porosities of: 0, 0.1, 0.3, 0.5 and 0.7, respectively). For all results shown in Figs. 4 and 5 the horizon size was 40 mm. Fig. 5 shows that higher porosity leads to lower wave propagation speed, as expected. In the IH-PD model, the pre-damage amount (corresponding to the given, input porosity) leads to this lower apparent modulus. In contrast, in FH-PD models, the lower input effective elastic modulus leads to this slowing in propagation of elastic waves in materials with higher and higher porosity.

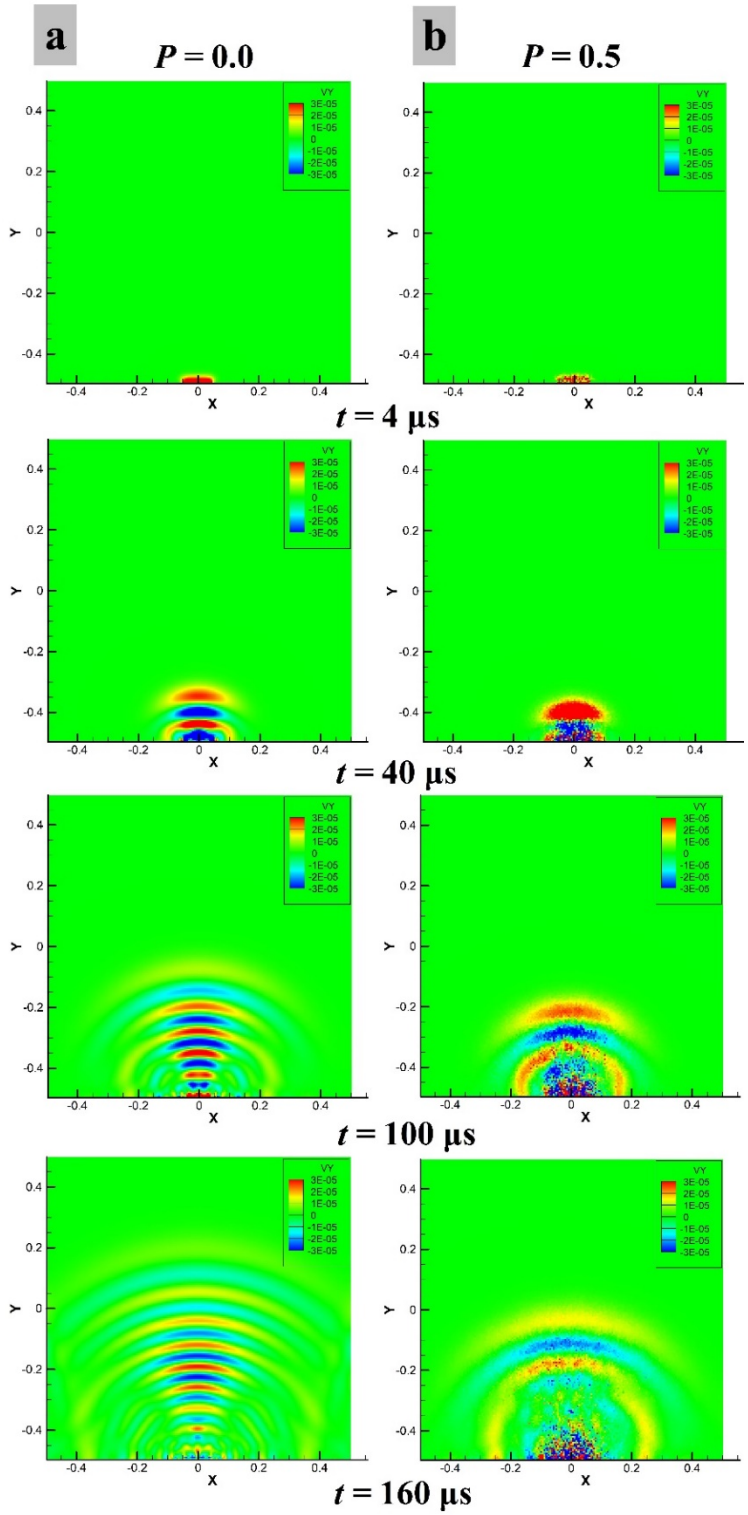

Fig. 4. The vertical component of the nodal velocity vector, showing the progression of wave propagation in time for porous and non-porous materials: (a) P = 0, (b) P = 0.5. See also movies 1 and 3.

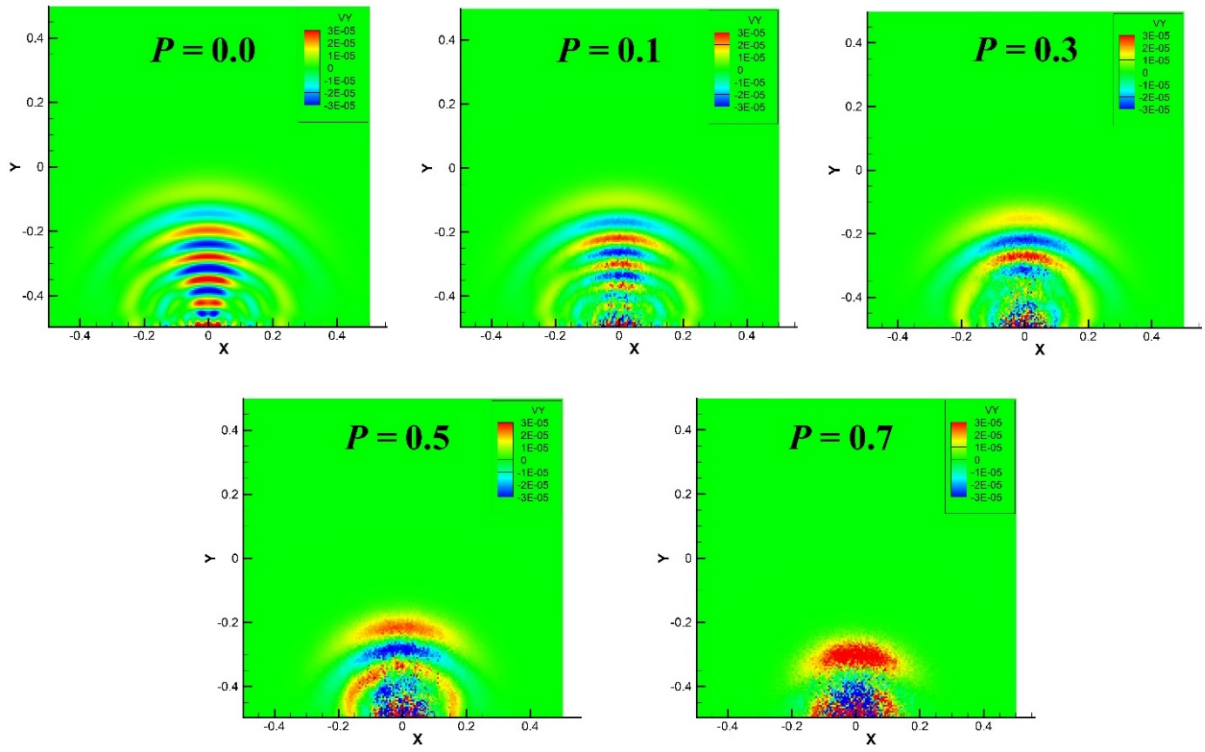

Fig. 5. The vertical component of the nodal velocity vector, showing the wave propagation at t = 100 μs for samples with different porosity P. See also movies 1-5.

We now study m-convergence and δ-convergence to see the influence of the horizon factor and nonlocal horizon size (δ) on the wave speed at different porosities.

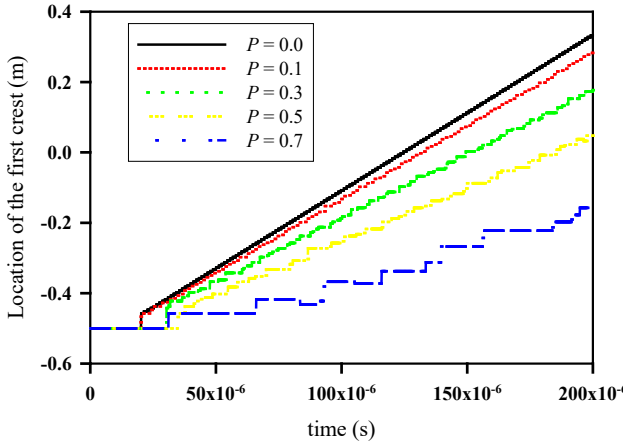

Fig. 6. Locations of the crest of the front wave versus time. Results obtained with a horizon size of 40 mm, and horizon factor m=8.

Fig. 7 presents the convergence results from the IH-PD model for elastic wave speed in the porous glass versus porosity. To calculate the wave speed, we compute an averaged velocity by tracking the location of the crest (along the line of $x = 0$) of the front wave during the time range100~200 μs from the application of the pulse load. Fig. 6 shows the crest locations versus time, for different porosities. We use a linear fit for the vertical velocity data points within the time range mentioned above to extract the wave speed velocity shown in Fig. 7, for each porosity.

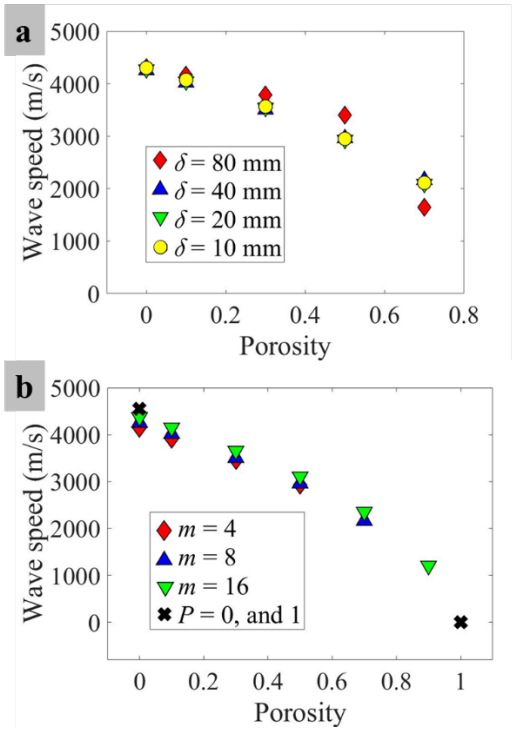

Fig. 7. Convergence results in terms of the pressure wave propagation speed for the porous glass versus porosity: (a) δ -convergence for m=8, and (b) m-convergence for δ = 40 mm.

As mentioned before, at high porosities, (0.7, 0.9), there is a relatively larger probability for peridynamic nodes to lose all of their connections with the surrounding nodes if m is relatively small, since the number of bonds is relatively small. This is the reason for which only the higher values of m are used in these cases (see Fig. 7b).

The results in Fig. 7 show that m = 4 is a safe choice for simulating elasto-dynamic problems

in porous materials with the IH-PD model when the porosity is smaller than 0.5 (relative to a critical porosity of 1).

The apparent elastic modulus in glass samples with different porosities was experimentally measured.[54] To compare the PD results with experimental measurements, we compute the apparent modulus (E_P) from the wave speeds numerically obtained in the IH-PD simulations above. Based on the theory of 2D (plane stress) wave propagation,[55] the relationship between longitudinal or pressure wave speed and the apparent elastic modulus (E_P) is:

$$C_L = \sqrt{\frac{E_P}{\rho(1-\nu^2)}} \tag{13}$$

where C_L is the longitudinal waves speed. In the computation, we use 1/3 as the Poisson ratio, because the Poisson's ratio value for bond-based peridynamic model in 2D under plane stress conditions is 1/3.[56] The apparent modulus calculated from Eq. (13) by using the wave speed computed with the PD model matches well the experimental measurements (see Fig. 8).

Fig. 8 shows the *m*-convergence for the normalized apparent modulus (E_P/E, where E is the modulus at zero porosity) of the porous glass versus porosity. The limit of *m*-convergence approaches asymptotically the following functional behavior: $\frac{E_P}{E} = (1 - P/P_c)^2$. Note that the pre-damage index introduced by the given porosity was $d_P = 1 - (1 - P/P_c)^2$. Combining these relationships leads to $d_P = 1 - \frac{E_P}{E}$, which matches the classical formula for damage from continuum damage mechanics theory.[57] This is another verification of the soundness of our proposed model.

Note that, in practice, one usually measures the apparent modulus, while the critical porosity is unknown (or the modulus/porosity relation does not follow the equation $\frac{E_P}{E} = (1 - P/P_c)^2$). In

such cases, one can use the apparent modulus value and apply the IH-PD model to generate the pre-damage induced by the existing porosity, according to the formula: $d_P = 1 - \frac{E_P}{E}$.

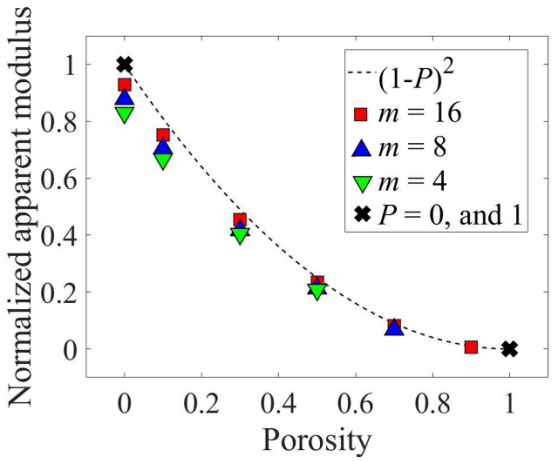

Fig. 8. Normalized apparent modulus for porous glasses versus porosity, computed from the IH-PD model results shown in Fig. 7. Critical porosity used here was taken as 1.

Fig. 9 compares the normalized apparent modulus obtained from the IH-PD model simulations with that from the experimental measurements.[7] In the IH-PD model, we select m = 16, and δ = 40 mm. The normalized modulus/porosity relationship obtained by the IH-PD model matches well the experimental measurements. The computations are able to test porosity values outside of those that can be manufactured, and in the limit of porosity converging to the critical porosity we confirm the virtual stopping of wave propagation in the medium.

With this model validation for elasto-dynamic problems, we next validate the IH-PD model for fracture using quasi-static fracture of a porous rock. We consider fracture induced by three-point bending of Berea sandstone.

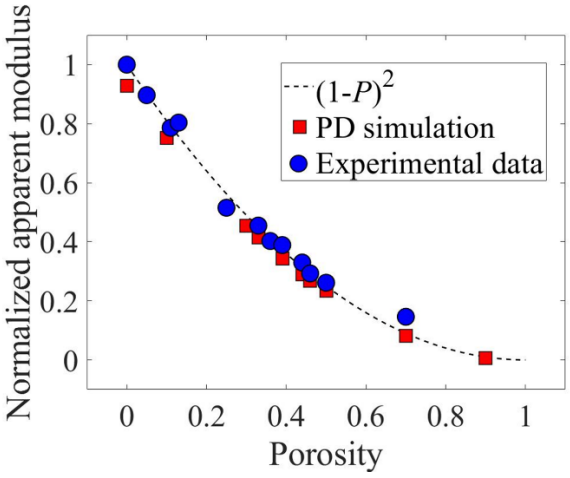

Fig. 9. Comparison between the IH-PD model results and experiments[54] for the apparent modulus/modulus ratio of porous glass (critical porosity taken as 1 in computations).

5. Peridynamic modeling of damage evolution in porous materials

We apply both the FH-PD and IH-PD models for quasi-static fracture of a porous rock sample. We find that only the IH-PD model delivers damage patterns and crack profiles similar to those seen in experiments in.[9]

5.1. Description of experimental setup and results, and of the numerical model

The experimental setup shown in Fig. 10 was used[9] for testing damage in Berea sandstone samples with an off-center notch and under quasi-static three-point bending. The experimental tests were conducted in specimens with notches of different lengths. The notch length determines the failure mode: when the notch is short (5.65 mm), the main crack initiates from near the beam's center and grows towards the loading point (see section 3.4 and Fig. 6 in Lin et al.[9]) in mostly mode I failure; when the notch is longer (12.23 mm), the beam fails by cracking from the tip of off-center; this crack grows at an angle towards the loading region on the top boundary (see section 3.4 and Fig. 8 in Lin et al.[9]) in mixed-mode. Fig. 7 in Lin et al.[9] also shows that for the long notch,

some damage, measured via acoustic emission (AE) and electronic speckle pattern interferometry (ESPI), is recorded near the beam's center. In what follows, we investigate whether the observed damage sensitivity to notch length are reproduced by any of the two PD models described in this paper.

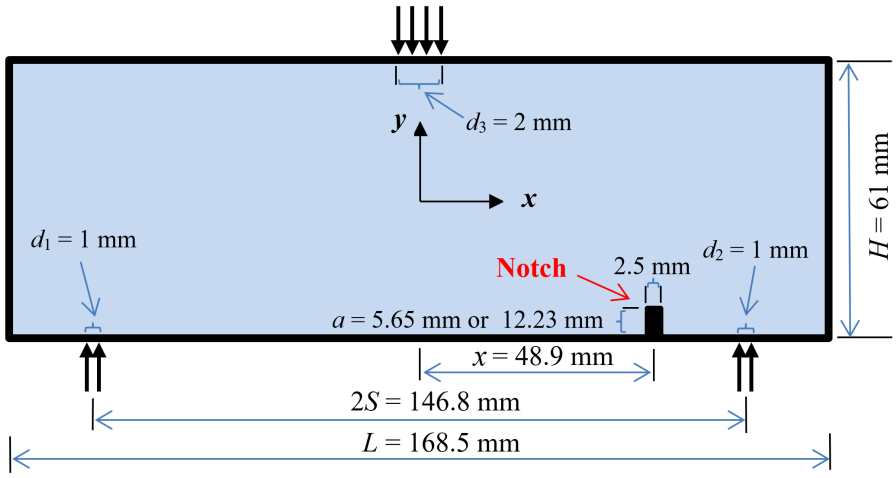

Fig. 10. Geometry and loading configuration[9] used in the peridynamic simulations.

In Lin et al.,[9] a discrete element model (the "slightly overlapped circular particles interaction" (SOCPI) model, see Fig. 3. in Fakhimi, et al.[58]) was used to simulate the failure process. In their model,[9] a synthetic rock is composed of rigid circular particles bonded together using normal and shear bonds at contact points (see Fig. 1. in Fakhimi[59]). Each contact bond breaks if the applied normal or shear contact force exceeds the corresponding normal or shear bond strengths. With the breakage of a bond, a Coulomb failure criterion is applied to a contact provided the contact is under a compressive normal loading. This contact bond model is defined by five microscopic parameters: normal and shear spring constants, normal and shear bonds, and a friction coefficient. Through the interaction of many rigid circular particles with given micromechanical properties, the macroscopic properties emerge. Hence, a process of trial and error is required to achieve appropriate macroscopic properties (e.g. Young's modulus) similar to those of a specific

rock, i.e., to calibrate the numerical model.[9] In section 5.3 we highlight advantages of our IH-PD model compared to the numerical model used by Lin et al.[9]

5.2. Problem setup

We consider the 2D problem of quasi-static crack growth in a notched Berea sandstone specimen under three-point bending loading. The geometry and boundary configuration used in experiments[9] and in our PD simulations are as shown in Fig. 10. Since the thickness of the specimen (26 mm) is small compared to its height and length, we model the problem as 2D plane stress. In experiments, the loading conditions were shown as point loads for the three-point bending tests, and no details about the size/shape of the loaded areas were given. Personal communication with Fakhimi[60] revealed the values shown in Fig. 10. Few details about the loading method were provided in Lin et al.[9], regarding both their experiments and simulations. Personal communication with Labuz[61], clarified that in experiments the crack mouth opening displacement (CMOD) was controlled with a constant rate of $1\sim2\times10^{-4}$ mm/s. This rate allows us to consider the crack growth as quasi-static in our model. From Fakhimi,[62] we found that the discrete element method simulations[9] used displacement-controlled conditions applied at the top middle points of the beam to simulate the three-point bending loading. We use a similar approach to represent the loading.

We will compare our PD simulation results with the experimental results in terms of fracture paths, locations of microcracks, and peak loads. These comparisons are not possible through full sample failure simply because the experimental results shown[9] stop before that. In our simulations, the imposed displacement is 2μm between increments. We run 2,000 increments to ensure full splitting of the samples.

Berea sandstone is chosen for our study because of its fairly uniform grain size,[9] which makes it a good candidate for the isotropic porosity model, as well as for its brittle failure behavior. Although Berea sandstone from different locations may have different porosities and thus different corresponding apparent moduli, we assume they all obey the relationship (see Section 4) $\frac{E_P}{E} = (1 - P/P_c)^2$, with critical porosity P_C and zero-porosity modulus E. The apparent fracture energy ($G_{0,P}$) has a similar relationship with porosity as the apparent modulus, thus $\frac{G_{0,P}}{G_0} = (1 - P/P_c)^2$.

In Lin et al.,[9] only the apparent modulus ($E_P = 10\sim12$ GPa) was mentioned, while other parameters (P, P_c, E, G_0, $G_{0,P}$) were not given. From Jaeger et al.,[34] we have the apparent modulus $E_P = 14.4$ GPa and a corresponding porosity P = 19% for a Berea sandstone sample. With these values and assuming a critical porosity of 40%[6], we calculate E = 52.24 GPa according to $\frac{E_P}{E} = (1 - P/P_c)^2$. For the sandstone beam used in Lin et al.,[9] we apply this modulus/porosity relationship to calculate its porosity. By assuming $E_P = 11$ GPa, we get the relative porosity $\frac{P}{P_c} = 54.1\%$.

Next, we determine the zero-porosity fracture energy, $G_{0,P}$. Measured values of Berea sandstone's apparent modulus ($E_P = 14$ GPa) and fracture toughness ($K_{\mathrm{IC}} = 0.3$ MPa m$^{1/2}$) have been reported in the literature.[63] The apparent fracture energy is found as $G_{0,P} = \frac{{K_{\mathrm{IC}}}^2}{E_P} = 6.43$ J/m^2 (for plane stress problems).[64] Since $\frac{G_{0,P}}{G_0} = \frac{E_P}{E} = (1 - P/P_c)^2$, we obtain $G_0 = 24$ J/m^2.

We use the material properties of the constituent material of the porous medium (E = 52.24 GPa and $G_0 = 24$ J/m^2) to calculate the bond information (micro-modulus and critical bond strain)

for the IH-PD model, with relative porosity $\frac{P}{P_c} = 54.1\%$. For the FH-PD model, we use the apparent mechanical properties: $E_P = 11$ GPa, $G_{0,P} = 5.05$ J/m^2.

For the two-dimensional bond-based peridynamic model of an isotropic and homogeneous material in plane-stress conditions, the Poisson ratio is 1/3. The Poisson ratio of the Berea sandstone varies between 0.3 and 0.35.[9] While Poisson's ratio can influence the path of a growing crack, these variations are not expected to play a significant role in the fracture behavior of porous rocks.[65] Peridynamic modeling of other poroelastic materials, for which bond-based model's fixed Poisson ratio does not happen to match as well, can be performed using the state-based peridynamic formulation.[47] The state-based PD formulation eliminates the Poisson ratio restriction. Because the Poisson ratio for the material considered here is close to 1/3 and the fact that our primary interest here is to observe the capabilities of a PD model in capturing the evolution of fracture and failure in poroelastic materials and to determine other factors that control crack growth in poroelastic materials, we use the bond-based peridynamic formulation. In our simulations, we use the conical micromodulus (see Eqs. (5) and (9)), $\delta = 2$ mm and $m = 4$.

5.3. Results and discussion

We use the FH-PD and IH-PD models (with the quasi-static loading conditions specified in the previous section) to simulate the cases shown in Fig. 10, and to examine the effect the pre-notch length has on the failure mode and crack patterns. In the IH-PD model, the effect of porosity is represented by inserting "pre-damage" in the material, while in the FH-PD model, porosity is indirectly represented by the apparent elastic and fracture properties.

Fig. 11 shows the simulation results generated by the IH-PD model in the short and long pre-notched Berea sandstone samples with $\frac{P}{P_c} = 54.1\%$. Figs. 11c and 11d show the damage maps due to mechanical damage only, without considering the pre-damage. The fracture paths seen from

these damage maps are consistent with the experimental findings on the effect of the notch length: the long pre-notch leads to crack initiating from the off-center pre-notch tip, while in the short pre-notch case, the crack initiates from the bottom-center of the beam.

Movies 6 and 7 show the damage evolution with and without pre-damage due to porosity, respectively, for the short pre-notched sample using the IH-PD model. Movies 8 and 9 show the damage evolution with and without pre-damage due to porosity, respectively, for the long pre-notched sample using IH-PD model. In movies 6-9, the imposed displacement of the top-center of beam progresses from 0 to 2.6 mm. In these movies, the damage quantity shown is scaled to a ^{64} range between 0 and 1, and the same is done for the rest of such movies.

As displayed in movies 6-9, our PD simulations track the crack growth through full failure, when the sample splits in two. The numerical results in Lin et al.,[9] are limited to the intermediate stages of crack growth and do not include the crack paths through final failure (see Figs. 10 and 12 in Lin et al.[9]). It is not clear whether this is a limitation of the model they used or the authors only wanted to track the reported experimental results, which also are only reported well before full splitting.

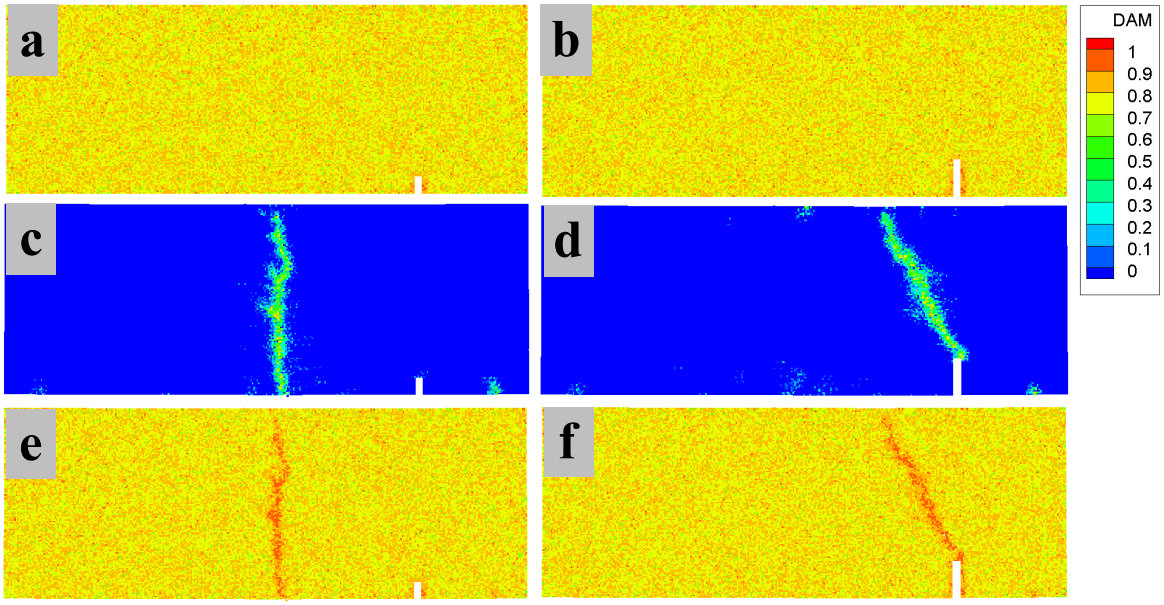

Fig. 11. Damage maps from IH-PD model simulation: Pre-damage maps in the short (a) and long (b) pre-notched samples; (c) and (d): fracture paths shown by mechanical damage due only to loading (pre-damage not shown) at the total imposed displacement of 0.4 mm at the beam's top-center; (e) and (f): damage maps from combining pre-damage with mechanical damage. Evolution of damage with increased loading is shown in movies 6-9.

Fig. 12 presents the damage index maps for the short and long pre-notched samples using the FH-PD model. The FH-PD model does not capture the influence of the pre-notch length on the crack initiation and propagation in the porous sample, observed experimentally. With the FH-PD model, the crack initiates from the tip of pre-notch, even in the short notch case.

Because of the simplifying assumptions implicit in a full homogenization of a porous material (absence of microscale heterogeneities and defects), the high stress concentration at the tip of preexisting notch, whether long or short, causes fracture to initiate (Fig. 12). In reality, small scale heterogeneities (presence of pores) result in local stress concentrations at places other than the off-center notch tip, and most likely in the regions near the bottom center of the beam where tensile bending stress is highest. This is what leads cracks to initiate from the beam's middle bottom rather than the pre-notch tip, in the short-notch case (Fig. 11c and 11e).

Movies 10 and 11 show the damage evolution for the short and long pre-notched samples, respectively, using the FH-PD model with conical micromodulus. In these simulations the imposed displacement at the top-center of beam progresses from 0 to 1.9 mm.

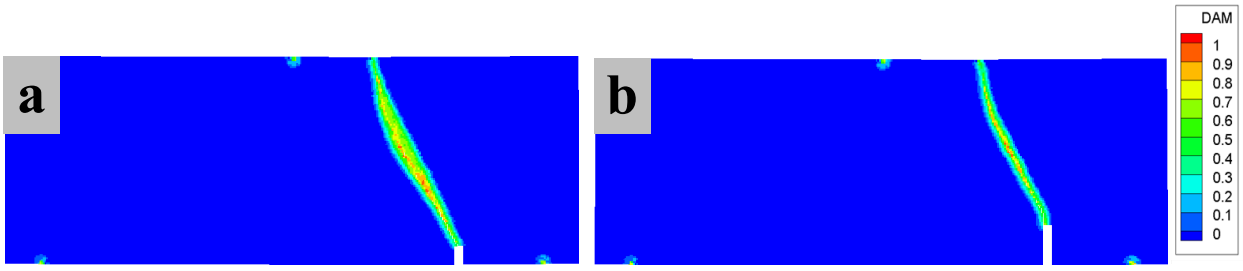

Fig. 12. Damage maps for the short (a) and long (b) pre-notch cases using the FH-PD model. See movies 10 and 11 for the evolution of damage.

To make it easier to analyze the computed damage distribution in the material, we blank the material nodes with damage index of zero in Fig. 13. The snapshots shown in Fig. 13 are at the applied displacement of 0.4 mm at the top-center of the beam, using the IH-PD (Figs. 13a and 13b) and FH-PD (Figs. 13c and 13d) models, respectively. Results obtained with the IH-PD model (Figs. 13a and 13b) match very well the experiments (see Fig. 3 in Lin et al.[9]). Note that the initiation of fracture in the specimen with the short notch is the same as that in the specimen without a notch (similar distribution of damage around the final crack path). Figs. 7 and 8 in Lin et al.[9] show that, experimentally, while for the long notch case the specimen fails from the notch tip, some damage is also recorded around the bottom center of the beam. As seen in Fig. 13b, the IH-PD model captures this micro-damage at the beam center for the long notch case, as observed in experiments, while the FH-PD model (Fig. 13d) does not.

Fig. 14 overlaps the data extracted from the numerical model and experiments used in Lin et al.[9], with the data produced by the IH-PD model for the long notch case. The available experimental results (red diamonds in Fig. 14) only show the early stages of the fracture process.

The peridynamic results (from the IH-PD model) match well with the acoustic emission data[9], showing damage accumulating at the right corner of the notch tip, while the numerical results from Lin et al.[9], show crack initiation from the left corner of the notch.

Movies 12 and 13 show the mechanical damage evolution (blanking nodes with zero mechanical damage index) for the short and long pre-notched samples, respectively, using IH-PD model. In movies 14 and 15, the mechanical damage evolution for the short and long pre-notched samples, respectively, using FH-PD model are displayed. In movies 12-15, the imposed displacement of the top-center of beam progresses from 0.6 μm to 0.4 mm.

The damage evolution for the long notch case solved with the IH-PD model (seen from movie 13) shows distributed damage around the beam bottom-center occurring earlier than the damage that eventually leads to full failure, starting at the pre-notch tip.

We note that the location of long notch shown in Figs. 7 and 8 in Lin et al.[9] is incorrect. Based on Table 2 in Lin et al.,[9] the notch is located at two-thirds of the half-span length (about 49 mm from the center, see Fig. 10); however, the notch is shown to be located close to 40 mm in Figs. 7 and 8 in Lin et al..[9] We use the parameter in Table 2 in Lin et al.,[9] which is also the data shown in their other paper.[58]

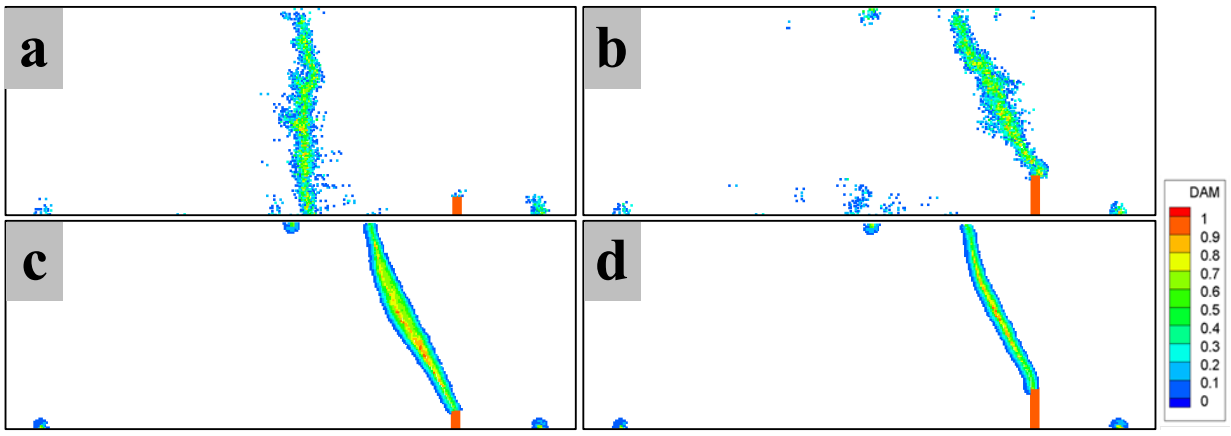

Fig. 13. Damage index maps resulting from mechanical damage (pre-damage and nodes with zero mechanical damage not shown). (a) and (b): IH-PD model with short and long pre-notch, respectively (see movies 12 and 13); (c) and (d): FH-PD model with short and long pre-notch, respectively (see movies 14 and 15). Red rectangles show notch geometry.

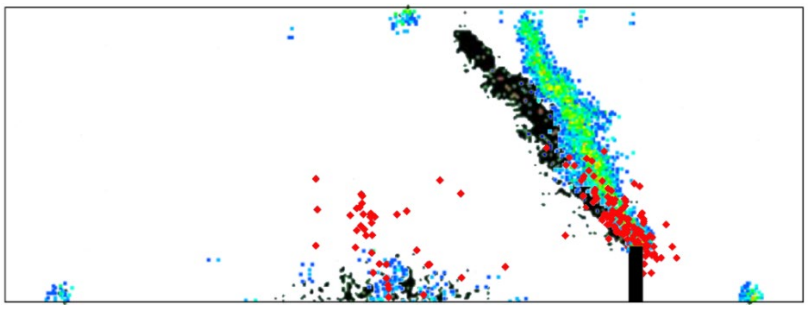

Fig. 14. Overlay of damage obtained by acoustic emission from Lin et al.[9] (red diamonds), the IH-PD model (multi-color squares, and using the legend in Fig. 13), and the numerical model in Lin et al.[9] (black dots). The off-center black rectangle shows the notch geometry and location.

In Table 1, we compare the peak loads (the maximum load values) reported in the experiments with those obtained with our models. The results from the IH-PD model match well the experimental data. The peak load obtained by FH-PD model for the short notch case deviates significantly from the experiments because of the different mode of failure obtained in this case.

Table 1. Comparison of peak load obtained from experiments with those from the peridynamic models

	Peak load/thickness by experiment[9]	Peak load/thickness by IH-PD model	Peak load/thickness by FH-PD model
Short notch	$59.535\,\frac{\mathrm{kN}}{\mathrm{m}}$	$49.952\,\frac{\mathrm{kN}}{\mathrm{m}}$ (Relative error=16%)	$77.476\,\frac{\mathrm{kN}}{\mathrm{m}}$ (Relative error=30.1%)
Long notch	$46.48\,\frac{\mathrm{kN}}{\mathrm{m}}$	$49.694\,\frac{\mathrm{kN}}{\mathrm{m}}$ (Relative error=6.9%)	$49.376\,\frac{\mathrm{kN}}{\mathrm{m}}$ (Relative error=6.2%)

Compared with the numerical model presented in Lin et al.,[9] the IH-PD model introduced here has following advantages:

i. The IH-PD model presented here uses only an elastic-and-brittle-failure model, matching the sandstone micro-scale behavior. The actual sandstone heterogeneities/porosity (represented in our model via pre-damage) lead to an effective, macroscale behavior that displays softening. In contrast, Lin et al.'s [9] use a softening contact bond model, in which the normal bond strength reduces linearly after its peak, to mimic the observed macroscale behavior.

ii. No trial-and-error calibration for material constants is necessary for the IH-PD model. In the IH-PD model, macroscopic measurable properties (e.g. porosity, etc.) are input parameters. On the other hand, the constitutive model in the contact bond model[9] is defined by many microscopic material constants. Through the interaction of many discrete element particles (with microscopic material constants), macroscopic properties emerge. Hence, trial and error steps (or calibration processes) are required to achieve appropriate macroscopic properties similar to those of a specific rock.

6. Conclusions

In this paper we presented an Intermediately-Homogenized Peridynamic (IH-PD) model for simulating the elastic and failure behavior of porous materials. In this model, porosity was represented by an initial peridynamic damage ("pre-damage"), introduced by breaking bonds, stochastically, to achieve a given porosity. The peridynamic micromodulus was computed using the elastic modulus of the porous medium constituent material. We validated the model for elastic wave propagation using experimental data for wave propagation speeds and the apparent elastic

moduli in porous glass with different porosities.

While simple homogenization methods work well for linear problems (e.g., elastic response), for nonlinear problems (e.g., in damage and failure), where dissipation and weakest links play a role in determining the material behavior, such methods may fail to reproduce experimental observations. To answer the question "how much homogenization is too much?" when modeling fracture processes in porous materials, we compared two peridynamic models: one that homogenized the material to a greater extent (the Fully-Homogenized Peridynamic model, FH-PD) and the newly introduced IH-PD model. We studied a quasi-static crack growth problem in a brittle porous rock to understand the difference between the models' responses. We found that the fully-homogenized model (FH-PD) failed to capture the experimentally observed fracture behavior in Berea sandstones sample under three-point bending loading. For this problem, experiments show that fracture patterns are controlled by the size of the off-center pre-notch. The IH-PD model, however, reproduced perfectly the observed crack growth behavior and its dependency on the length of the pre-notch.

We conclude that for problems in which the microstructure has a large effect on the failure behavior, a fully homogenized strategy will not work to correctly capture the fracture and damage evolution. For a predictive model, some of the details of the microstructure and its role in controlling crack growth are needed. The new IH-PD model can predict the correct failure evolution in a porous material without requiring the explicit description of the microstructure geometry. This happens because some essential features (porosity represented via peridynamic pre-damage) of the material microstructure are incorporated in the model. It is this extra microstructure information that allows the computed damage to initiate and evolve in a way similar to that in the real porous medium.

Acknowledgements:

This work was supported by a grant from ONR (program manager: William Nickerson) and by the AFOSR MURI Center for Material Failure Prediction through Peridynamics (program managers: Drs. Jaimie Tiley, David Stargel, Ali Sayir, Fariba Fahroo, and James Fillerup). This work was completed utilizing the Holland Computing Center of the University of Nebraska, which receives support from the Nebraska Research Initiative.

References:

1. Biot MA. General theory of three‐dimensional consolidation. *J Appl Phys.* 1941;12(2): 155-164.

2. Cheng AHD. *Poroelasticity*: Springer; 2016.

3. Coussy O. *Mechanics of porous continua*: Wiley; 1995.

4. Nur A, Mavko G, Dvorkin J, Galmudi D. Critical porosity: A key to relating physical properties to porosity in rocks. *Lead Edge.* 1998;17(3): 357-362.

5. Nolen-Hoeksema RC. Modulus—porosity relations, Gassmann's equations, and the low-frequency elastic-wave response to fluids. *Geophys.* 2000;65(5): 1355-1363.

6. Dvorkin J, Nur A. Critical-porosity models. *Mem Am Assoc Pet Geol.* 2002: 33-42.

7. Manoylov A, Borodich FM, Evans HP. Modelling of elastic properties of sintered porous materials. *Proc R Soc London Ser A.* 2013;469(2154): 20120689.

8. Kaczmarek M, Goueygou M. Dependence of elastic properties of materials on their porosity: Review of models. *J Porous Media.* 2006;9(4): 335-355.

9. Lin Q, Fakhimi A, Haggerty M, Labuz JF. Initiation of tensile and mixed-mode fracture in sandstone. *Int J Rock Mech Min Sci.* 2009;46(3): 489-497.

10. Haggerty M, Lin Q, Labuz J. Observing deformation and fracture of rock with speckle patterns. *Rock Mech Rock Eng.* 2010;43(4): 417-426.

11. Zhang H, Fu D, Song H, Kang Y, Huang G, Qi G, Li J. Damage and fracture investigation of three-point bending notched sandstone beams by DIC and AE techniques. *Rock Mech Rock Eng.* 2015;48(3): 1297-1303.

12. Mohammadnejad M, Liu H, Chan A, Dehkhoda S, Fukuda D. An overview on advances in computational fracture mechanics of rock. *Geosyst Eng.* 2018: 1-24.

13. Dormieux L, Jeannin L, Gland N. Homogenized models of stress-sensitive reservoir rocks. *Int J Eng Sci.* 2011;49(5): 386-396.

14. Liu W, Chen YF, Hu R, Zhou W, Zhou CB. A two-step homogenization-based permeability model for deformable fractured rocks with consideration of coupled damage and friction effects. *Int J Rock Mech Min Sci.* 2016;89: 212-226.

15. Silling SA. Reformulation of elasticity theory for discontinuities and long-range forces. *J Mech Phys Solids.* 2000;48(1): 175-209.

16. Silling SA, Lehoucq RB. Convergence of peridynamics to classical elasticity theory. *J Elast.* 2008;93(1): 13-37.

17. Bobaru F, Ha YD, Hu W. Damage progression from impact in layered glass modeled with peridynamics. *Cent Eur J Eng.* 2012;2(4): 551-561.

18. Chen Z, Bobaru F. Peridynamic modeling of pitting corrosion damage. *J Mech Phys Solids.* 2015;78: 352-381.

19. Cheng Z, Zhang G, Wang Y, Bobaru F. A peridynamic model for dynamic fracture in functionally graded materials. *Compos Struct.* 2015;133: 529-546.

20. Mehrmashhadi J, Tang Y, Zhao X, Xu Z, Pan J, Van Le Q, Bobaru F. The effect of solder joint microstructure on the drop test failure: a peridynamic analysis. *IEEE Trans Compon Packag Manuf Technol.* 2018.

21. Silling SA, Bobaru F. Peridynamic modeling of membranes and fibers. *Int J Nonlinear Mech.* 2005;40(2): 395-409.

22. Zhang G, Bobaru F. Modeling the evolution of fatigue failure with peridynamics. *Rom J Tech Sci Appl Mech.* 2016;66: 20-39.

23. Zhao J, Chen Z, Mehrmashhadi J, Bobaru F. Construction of a peridynamic model for transient advection-diffusion problems. *Int J Heat Mass Transfer.* 2018;126: 1253-1266.

24. Katiyar A, Foster JT, Ouchi H, Sharma MM. A peridynamic formulation of pressure driven convective fluid transport in porous media. *J Comput Phys.* 2014;261: 209-229.

25. Jabakhanji R, Mohtar RH. A peridynamic model of flow in porous media. *Adv Water Resour.* 2015;78: 22-35.

26. Turner DZ. A non-local model for fluid-structure interaction with applications in hydraulic fracturing. *Int J Comput Methods Eng Sci Mech.* 2013;14(5): 391-400.

27. Ouchi H, Katiyar A, York J, Foster JT, Sharma MM. A fully coupled porous flow and geomechanics model for fluid driven cracks: a peridynamics approach. *Comput Mech.* 2015;55(3): 561-576.

28. Nadimi S, Miscovic I, McLennan J. A 3D peridynamic simulation of hydraulic fracture process in a heterogeneous medium. *J Petrol Sci Eng.* 2016;145: 444-452.

29. Zhou XP, Gu XB, Wang YT. Numerical simulations of propagation, bifurcation and coalescence of cracks in rocks. *Int J Rock Mech Min Sci.* 2015;80: 241-254.

30. Wang Y, Zhou X, Shou Y. The modeling of crack propagation and coalescence in rocks under uniaxial compression using the novel conjugated bond-based peridynamics. *Int J Mech Sci.* 2017;128: 614-643.

31. Wang Y, Zhou X, Wang Y, Shou Y. A 3-D conjugated bond-pair-based peridynamic formulation for initiation and propagation of cracks in brittle solids. *Int J Solids Struct.* 2018;134: 89-115.

32. Zhou X, Wang Y, Xu X. Numerical simulation of initiation, propagation and coalescence of cracks using the non-ordinary state-based peridynamics. *Int J Fract.* 2016;201(2): 213-234.

33. Lee J, Ha YD, Hong J-W. Crack coalescence morphology in rock-like material under compression. *Int J Fract.* 2016: 1-26.

34. Jaeger JC, Cook NGW, Zimmerman RW. *Fundamentals of rock mechanics.* Fourth ed: Blackwell Publishing; 2007.

35. Cui ZD, Liu DA, An GM, Sun B, Zhou M, Cao FQ. A comparison of two ISRM suggested chevron notched specimens for testing mode-I rock fracture toughness. *Int J Rock Mech Min Sci.* 2010;47(5): 871-876.

36. Manger GE. Porosity and bulk density of sedimentary rocks. USGPO; 1963.

37. Bernabe Y, Brace W. Deformation and fracture of Berea sandstone. *The brittle-ductile transition in rocks.* 1990: 91-101.

38. Renner J, Evans B, Hirth G. On the rheologically critical melt fraction. *Earth Planet Sci Lett.* 2000;181(4): 585-594.

39. Silling SA, Epton M, Weckner O, Xu J, Askari E. Peridynamic states and constitutive modeling. *J Elast.* 2007;88(2): 151-184.

40. Bobaru F, Yang M, Alves LF, Silling SA, Askari E, Xu J. Convergence, adaptive refinement, and scaling in 1D peridynamics. *Int J Numer Methods Eng.* 2009;77(6): 852-877.

41. Ha YD, Bobaru F. Studies of dynamic crack propagation and crack branching with peridynamics. *Int J Fract.* 2010;162(1): 229-244.

42. Chen ZG, Bakenhus D, Bobaru F. A constructive peridynamic kernel for elasticity. *Comput Methods Appl Mech Eng.* 2016;311: 356-373.

43. Xu ZP, Zhang GF, Chen ZG, Bobaru F. Elastic vortices and thermally-driven cracks in brittle materials with peridynamics. *Int J Fract.* 2018;209(1-2): 203-222.

44. Silling SA, Askari E. A meshfree method based on the peridynamic model of solid mechanics. *Comput Struct.* 2005;83(17-18): 1526-1535.

45. Hu W, Ha YD, Bobaru F. Numerical integration in peridynamics. *Technical report.* Lincoln: University of Nebraska-Lincoln; 2010.

46. Bobaru F, Zhang GF. Why do cracks branch? A peridynamic investigation of dynamic brittle fracture. *Int J Fract.* 2015;196(1-2): 59-98.

47. Shewchuk JR. An introduction to the conjugate gradient method without the agonizing pain. *Technical report.* Pittsburgh: School of Computer Science, Carnegie Mellon University; 1994.

48. Zhang GF, Le Q, Loghin A, Subramaniyan A, Bobaru F. Validation of a peridynamic model for fatigue cracking. *Eng Fract Mech.* 2016;162: 76-94.

49. Chen Z, Niazi S, Zhang G, Bobaru F. Peridynamic Functionally Graded and Porous Materials: Modeling Fracture and Damage. *Handbook of Nonlocal Continuum Mechanics for Materials and Structures.* Springer; 2018:1-35.

50. Chen ZG, Zhang GF, Bobaru F. The Influence of Passive Film Damage on Pitting Corrosion. *J Electrochem Soc.* 2016;163(2): C19-C24.

51. Li SM, Chen ZG, Wang F, Cui B, Tan L, Bobaru F. Analysis of Corrosion-Induced Diffusion Layer in ZK60A Magnesium Alloy. *J Electrochem Soc.* 2016;163(13): C784-C790.

52. Jafarzadeh S, Chen Z, Bobaru F. Peridynamic modeling of repassivation in pitting corrosion of stainless steel. *Corros.* 2017;74(4): 393-414.

53. Jafarzadeh S, Chen Z, Bobaru F. Peridynamic Modeling of Intergranular Corrosion Damage. *J Electrochem Soc.* 2018;165(7): C362-C374.

54. Walsh JB, Brace WF, England AW. Effect of porosity on compressibility of glass. *J Am Ceram Soc.* 1965;48(12): 605-608.

55. Johnson W. Impact strength of materials. 1972.

56. Quang L, Bobaru F. Objectivity of state-based peridynamic models for elasticity. *J Elast.* 2018;131(1): 1-17.

57. Lemaitre J. *A course on damage mechanics*. Berlin: Springer; 1992.

58. Fakhimi A, Lin Q, Haggerty M, Labuz J. Development of fracture in bending experiments. *Alaska Rocks 2005, The 40th US Symposium on Rock Mechanics (USRMS), .* American Rock Mechanics Association; 2005.

59. Fakhimi A. Application of slightly overlapped circular particles assembly in numerical simulation of rocks with high friction angles. *Eng Geol.* 2004;74(1): 129-138.

60. Fakhimi A. Personal Communication. June 15, 2016.

61. Labuz JF. Personal Communication. August 1, 2017.

62. Fakhimi A. Personal Communication August 8, 2016.

63. Chen L, Labuz J. Indentation of rock by wedge-shaped tools. *Int J Rock Mech Min Sci.* 2006;43(7): 1023-1033.

64. Zhou X, T.L. *Fracture Mechanics: Fundamentals and Applications*: CRC Press; 2005.

65. Delale F, Erdogan F. The crack problem for a nonhomogeneous plane. *ASME J Appl Mech.* 1983;50(3): 609-614.